Variability Analysis of a Simulated CTAO Dataset on the TeV Blazar Markarian 421
REU Program at Columbia University - Nevis Labs

Owen Coffey[1]

[1]SUNY Geneseo

August 10, 2025

Abstract

The Cherenkov Telescope Array Observatory (CTAO) is the next-generation ground-based gamma-ray observatory, and is currently under construction. While it is being built, the Science Data Challenge (SDC) was released internally by the collaboration to develop analysis pipelines for CTAO data using Gammapy, a Python package for gamma-ray astronomy. Blazars are a class of jetted Active Galactic Nuclei that make up the majority of known extragalactic TeV gamma-ray sources. Minute-timescale variability has been observed in a variety of blazars but lacks a concrete explanation. Markarian 421 is a nearby blazar that has exhibited such variability. This study analyzed one year of simulated CTAO data from the SDC to assess the variability of the source on a variety of timescales and search for short-timescale variability. Variability was assessed using a statistical test, and the average variability probability was found to decrease over smaller time intervals. Unfortunately, the dataset was too sparse to determine a threshold timescale for the average variability probability to be significant. However, a conclusion can be made that CTAO should observe Markarian 421 for more than 30 minutes per week. Additionally, some instances of significant short-timescale variability were observed, and their characteristic timescales were assessed.

Contents

1 Introduction **2**
- 1.1 Gamma-Ray Astronomy . . . 2
- 1.2 IACTs . . . 2
  - 1.2.1 Detection Technique . . . 2
  - 1.2.2 CTAO . . . 3
- 1.3 Blazars . . . 3
  - 1.3.1 Gamma-Ray Emission in Blazars . . . 4
  - 1.3.2 Particle Acceleration . . . 4
- 1.4 Motivations . . . 5
  - 1.4.1 The CTAO Science Data Challenge and Gammapy . . . 5
  - 1.4.2 Variability Studies . . . 5
  - 1.4.3 Markarian 421 . . . 5

2 Dataset **6**

3 Analysis **6**
- 3.1 Gammapy Workflow . . . 6
- 3.2 Preliminary Analysis . . . 6
  - 3.2.1 Data Reduction . . . 6
  - 3.2.2 Point-Source Background Validation . . . 7
  - 3.2.3 Spectral Fitting and Flux Points . . . 7
- 3.3 Variability Analysis . . . 8
  - 3.3.1 Goals . . . 8
  - 3.3.2 Testing for Variability . . . 9
  - 3.3.3 Long Timescales . . . 9
  - 3.3.4 Short Timescales . . . 9
  - 3.3.5 Results . . . 11
  - 3.3.6 Special Cases . . . 11

4 Conclusions **14**
- 4.1 Variability Analysis . . . 14
- 4.2 Special Cases . . . 14

5 Acknowledgements **15**

1 Introduction

1.1 Gamma-Ray Astronomy

The cosmic ray spectrum has been well measured [19], and is shown in Fig. 1. The low-energy end of the spectrum is well understood, but a small flux of very high energy cosmic rays have energies than can only be generated by extreme cosmic particle accelerators. However, we cannot use cosmic rays to study these accelerators directly because charged particles will be deflected by intergalactic magnetic fields. Instead, we must use charge-neutral messengers like photons, in this case specifically high-energy gamma rays, or neutrinos.

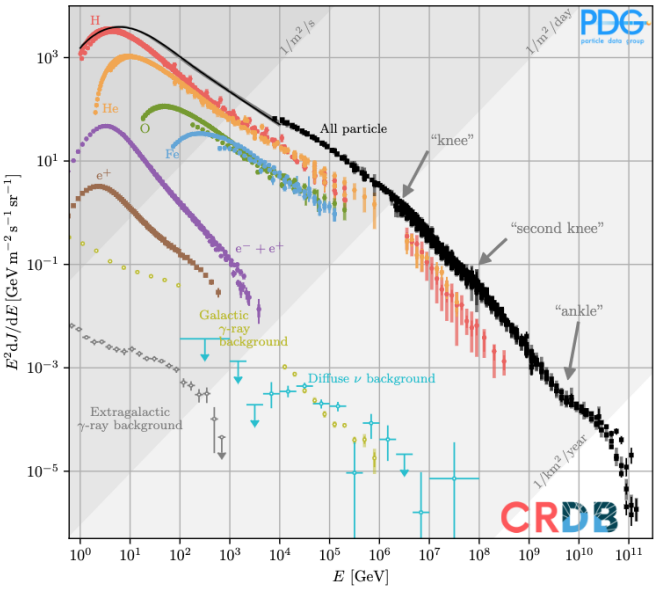

Figure 1: *The cosmic ray spectrum, plotted using data from the Cosmic Ray Database. The spectrum is well-represented by a power law with changes in slope near features known as the knee and ankle [19]*

1.2 IACTs

1.2.1 Detection Technique

Imaging Air Cherenkov Telescopes (IACTs) are the best ground-based method for detecting gamma rays in the Very High Energy (VHE) or TeV range. The atmosphere is unfortunately opaque to gamma rays. When a cosmic gamma ray interacts with an atomic nucleus in the atmosphere, it undergoes pair production, which generates a particle cascade of relativistic electrons and positrons. These particles move at incredibly high speeds, faster than the speed of light in air. When charged particles move faster than the speed of light in a medium, they emit Cherenkov light, in a manner similar to a sonic boom, where light waves bunch up in a cone behind the particle. The particles in extensive air showers produce a large pool of Cherenkov light, on the order of hundreds of square meters, detectable from the ground by extremely sensitive optical telescopes. Multiple telescopes within the light pool then allow for stereoscopic imaging of the shower, and reconstruction of it true origin point in the sky. The largest source of background in IACTs come from cosmic rays, which also initiate particle showers in the atmosphere. However, proton interactions with atmospheric nuclei produce different particles than gamma-ray interactions, and they generate very different particle cascades. For example, neutral pions generated in the collision will almost immediately decay into gamma rays, creating sub-showers, and muons will move quickly to the ground, generating their own small Cherenkov light pools.This results in air

showers with much more transverse momentum and a much less uniform shape than gamma-ray showers, which typically allows for easy manual rejection. However, due to the large volume of cosmic ray events, many are still misidentified, and serve as background that must be accounted for in analysis [13]. The Very Energetic Radiation Imaging Telescope Array System (VERITAS) is an example of a current-generation IACT. VERITAS is located in Southern Arizona, optimized to observe gamma-rays in the energy range between 85 GeV and 30 TeV [15].

1.2.2 CTAO

The Cherenkov Telescope Array Observatory (CTAO) is the next-generation IACT observatory, currently under construction. It will boast an exceptionally wide energy range, from as low as 20 GeV to as high as 300 TeV [16]. This is because CTAO will utilize 3 telescope designs, small, medium, and large, all optimized for different energy ranges. Novel telescope designs as well as larger arrays will give CTAO a factor of ten higher sensitivity in its optimal energy range than last-generation instruments, as shown in Fig 2, as well as better angular resolution [16]. Additionally, CTAO consists of two arrays, one in the Northern Hemisphere on La Palma in the Canary Islands, and one in the Southern Hemisphere in the Atacama Desert in Chile. Arrays in both hemispheres will give CTAO full-sky coverage [16].

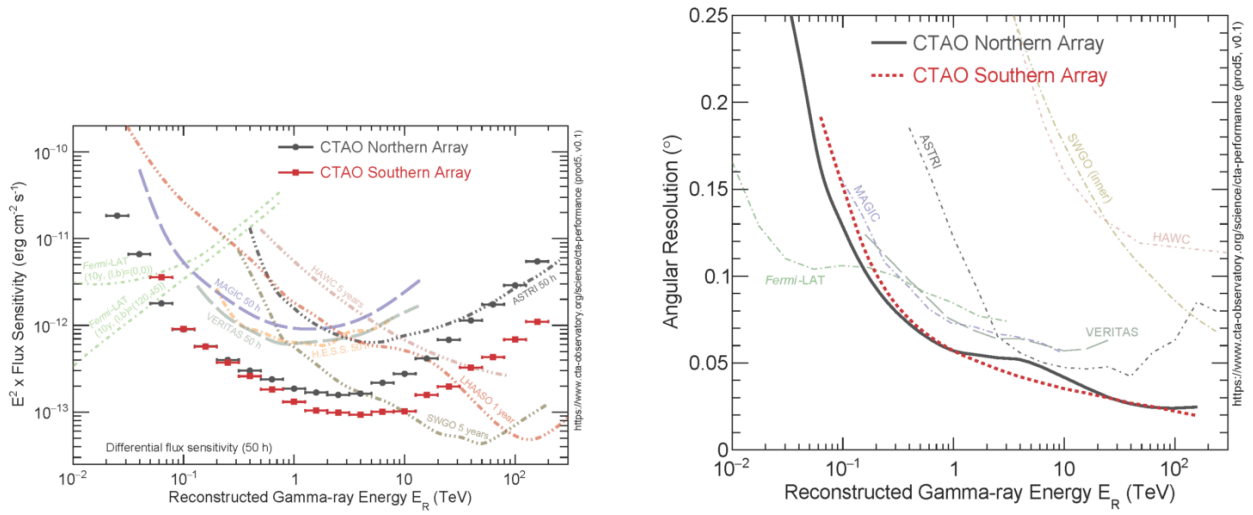

Figure 2: *Projected technical performance of CTAO compared to current-generation gamma-ray instruments [16].*

1.3 Blazars

Active Galactic Nuclei (AGN) are some of the brightest and oldest observable objects in the universe. AGN are Supermassive Black Holes at the center of galaxies that are actively accreting matter. These objects are typically very bright, and often outshine their host galaxies [10]. Matter falling into the black hole forms an accretion disk and a variety of characteristic structures, depicted in Fig. 3. The extreme magnetic fields formed by the accretion disk can occasionally lead to the generation of highly collimated jets of relativistic plasma. Depending on the viewing angle, presence of these jets, and the power of the central engine, the system can look very different. Originally, these appearances were thought to be different objects, but have since been classified as different views of the same type of object in the Unified Model of AGN [8]. Most important for gamma-ray astronomy are blazars, which are the type of object seen when an AGN's relativistic jets are pointed directly at the observer.

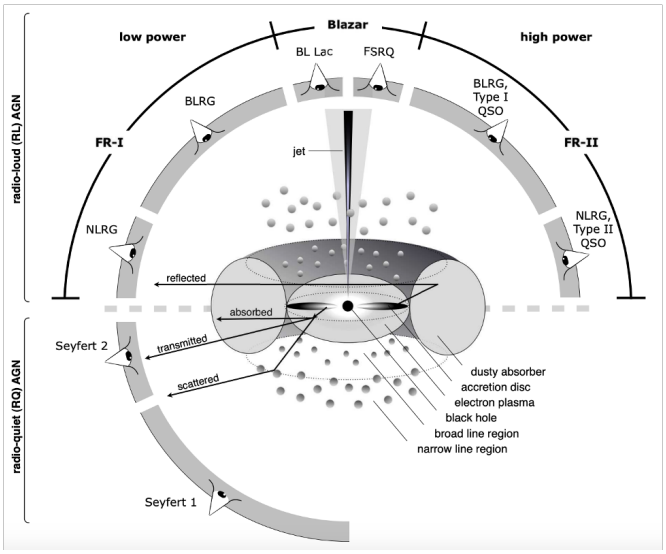

Figure 3: *Diagram of the unified model of AGN. The type of object seen depends on viewing angle, the presence of jets, and the accretion rate of the central black hole [8]*

1.3.1 Gamma-Ray Emission in Blazars

The spectral energy distribution (SED) of blazars is dominated by non-thermal emission and exhibits a characteristic double-peaked structure. This non-thermal emission comes from particle-level processes, by either leptons (electrons and positrons) or hadrons (protons). The lower peak of the SED, usually in the UV to X-ray range, is explained by synchrotron emission, either by electrons in the leptonic model or protons in the hadronic model. In the leptonic model, the higher peak, in gamma-rays, is explained by Inverse Compton Scattering, where high-energy electrons upscatter low-energy photons to high energies. The most common model is known as Self-Synchrotron Compton (SSC), where electrons upscatter their own synchrotron synchrotron emission by Inverse Compton Scattering. In the hadronic model, gamma-ray emission is dominated by neutral pion decay, produced by photon-proton interactions [10].

It is also understood that non-thermal emission observed from blazars originates in relativistic spherical "blobs" within the jets [22]. Since the blob is moving at relativistic speeds towards the observer, the emission is boosted due to the relativistic Doppler effect. This causes the emission to be boosted in intensity, explaining the AGN's high luminosity [8]. This effect is quantified by the Doppler factor, δ, defined as

$$\delta = \frac{1}{\Gamma(1 - \beta \cos\theta)}, \tag{1}$$

where θ is the viewing angle and Γ is the Lorentz factor. The Lorentz factor is defined as $\Gamma = 1/\sqrt{1 - (\frac{v}{c})^2}$, where v is the velocity of the emitting region and c is the speed of light in a vacuum.

1.3.2 Particle Acceleration

The source of particle acceleration in the jets, and therefore the source of variability in blazar light curves, is still very uncertain. The most well-established model is based around fluid dynamic shocks that form within the jets, which can be used to accelerate particles. However, to accelerate particles up to the energies necessary for gamma-ray emission, the particles often need to cross these shocks multiple times, which take too long to explain some of the minute-scale variability that has been observed in a few blazars [22]. However, a model plasmoid emission regions generated by magnetic reconnections in the jets is emerging to explain this short-timescale variability. In this model, turbulent flow of plasma generates opposing magnetic fields, which snap back together, releasing a large amount of energy and generating small plasmoids that can

act as gamma-ray emitting regions. This model has been shown to be capable of generating light curves with minute-timescale variability, although it is still being developed [18].

1.4 Motivations

1.4.1 The CTAO Science Data Challenge and Gammapy

Historically, gamma-ray astronomy has been conducted using proprietary data and analysis tools. CTAO, however, will be an open observatory, releasing its data to the public after a proprietary period. Therefore, if the data is publicly available, there should also be a publicly available toolkit to analyze that data. Gammapy, an open-source Python package for gamma-ray astronomy, was created in response to this need [12]. While the observatory is being built, the collaboration also saw the need to create a way to introduce the wider community to the data that CTAO will produce and the tools used to analyze it, and developed the Science Data Challenge (SDC). The SDC is a set of simulated data for a variety of different sources, including long term monitoring of AGNs, follow-ups on transient events like gravitational wave and neutrino detections, and more. Currently, the SDC is limited to members of the collaboration, with the intention of developing analysis pipelines for CTAO data with Gammapy and ensuring that the SDC is working correctly before it is released to the public next year [21]. My project analyzed the variability in the simulated long-term monitoring dataset for Markarian 421. It continues the work of Alex Sidler [7], a Nevis REU student from Summer 2024. While Sidler focused on detection, skymaps, and spectral modeling, my work focused on the variability of one of the sources he analyzed.

1.4.2 Variability Studies

Short-timescale variability has been observed in a variety of blazars [14] [3] [5] [2]. However, the mechanisms that cause these fast flares are still unclear, although new explanations are emerging. It is therefore valuable to gather as much data about short-timescale variability as possible, and optimize observation schedules to increase the chances of observing this short-timescale variability. Collecting more data will provide more materials for comparison with theoretical models, and shed light on the gamma-ray emission mechanisms in blazars. For example, the size of the emission region can be constrained using the variability timescale using equation

$$R = \frac{ct_{var}\delta}{1+z}, \tag{2}$$

where R is the radius of the spherical emission region, t_{var} is the variability timescale, δ is the Doppler factor and z is the redshift of the source. This variability study sought to determine the optimal timescale on which CTAO can observe short-term variability in the blazar Markarian 421.

1.4.3 Markarian 421

Markarian 421 is a nearby blazar at a redshift of $z = 0.031$. It is the closest BL Lac object, the lower-luminosity subclass of blazars, compared to Flat Spectrum Radio Quasars (FSRQs), the other subclass [3]. It was also the first extragalactic TeV source ever detected, by Whipple in 1992 [20]. Additionally, Markarian 421 has a history of very short-timescale variability. In 1996, it became the brightest TeV source in the sky over the course of an hour [14]. More recently, in 2010, VERITAS observed the largest flare to date, which also contained two very short bursts over the course of approximately two hours [3]. Mrk 421's history of short-timescale variability therefore makes it a great candidate for probing CTAO's ability to detect variability on these short timescales. For this project Markarian 421's 1-year light curve was tested for variability over a variety of time intervals, seeking the shortest timescale on which significant variability could be detected. Additionally, the light curve was searched for any short-timescale flaring activity.

2 Dataset

The simulated data used in this project were taken from the internal release of CTAO's 2nd SDC. It contains 118 total observations of Markarian 421 stored as preprocessed FITS files, which contain both event data (gamma-ray counts) and Instrument Response Functions (IRFs). IRFs characterize the performance of the telescope and are used for reconstructing the true energy and source position of the detected gamma rays. Each observation is 7.5 minutes long, and they are grouped into four consecutive observations for 30-minute observing runs. These observing runs take place once a week for a year (in 2028), with a gap from July to October when the source is not visible.

3 Analysis

3.1 Gammapy Workflow

Gammapy is an open-source, community-developed Python package built for gamma-ray astronomy. Alongside being built specifically for use with CTAO, it is being developed with the goal of unifying the analysis pipelines for all gamma-ray instruments. Therefore, nearly all analyses with Gammapy have a common workflow. In general, Gammapy accepts Data Level 3 (DL3) FITS files containing reconstructed energy and position data for the events, as well as IRF information. Gammapy then reduces those events into data binned along energy, spatial, and/or time axes (DL4), before turning that data into science products like spectra, skymaps, and light curves (DL5) [12]. Through this section, more details of this process will be described via explanation of the analysis of Markarian 421.

3.2 Preliminary Analysis

Before performing the variability analysis, it was important to conduct a preliminary analysis, confirming detection of the source and fitting a spectral model, which is necessary for estimating the flux.

3.2.1 Data Reduction

Before performing science analysis, the data needed to be reduced with a set of analysis selections that defined the science region of interest. The DL3 files were first brought into Gammapy as Observation objects, which are selected from the SDC DataStore with a 5-degree cut around the known position of the source. These contain information about the counts and observation-specific IRFs. It is commonly assumed that the instrument response can be represented as the product of three functions [12],

$$R(p, E|p_{true}, E_{true}) = A_{eff}(p_{true}, E_{true}) \cdot PSF(p|p_{true}, E_{true}) \cdot E_{disp}(E|p_{true}, E_{true}). \quad (3)$$

$A_{eff}(p_{true}, E_{true})$ is the effective collection area of the detector, defined as the product of the detector collection area and its detection efficiency at p_{true}, E_{true}. The effective area typically decreases towards the edges of an instruments energy range. The PSF, or Point Spread Function describes the probability density of measuring a position p when the true position and energy are p_{true} and $, E_{true}$. Effectively, it describes how spread out a point source will appear in the data. Finally, $E_{disp}(E|p_{true}, E_{true})$ is the energy dispersion, and gives the probability of accurately reconstructing a photon with true energy E_{true} and position p_{true} at energy E [12]. These are taken into account in the transitions to higher Data Levels.

Once the observations were selected, the data reduction was performed. Since Markarian 421 is a point source a 1D analysis was necessary, as we are only concerned with the energy dimension.

The energy axis was defined with 10 bins on a logarithmic scale between 10 GeV and 10 TeV, covering the entire energy range of CTAO North. The ON region was defined to be a 0.1° circle around the source position, which is typical for point sources. To estimate the background, I used the Reflected Regions background method [9], which is used for point-source analysis. It relies on the "wobble" observation method, in which the telescope "wobbles" ±0.5° off the source to capture both the source and background in the FOV. This method has the advantage of not requiring extra observations for background sampling, canceling out any systematic effects in the background estimation like changes in weather or performance [6]. The reflected regions method then reflects the source region onto many small regions in the background at the same radial distance from the center of the observation, and the background is measured within those regions. Since the OFF regions are all at the same distance from the center of the FOV, no radial acceptance correction is required [9]. Exclusions masks are placed over any gamma-ray source or bright star in the field of view. In this case, a 0.3°-radius exclusion region was placed over the source to prevent source contamination of the background. The geometry for the background estimation is shown in Fig. 4

The excess counts are calculated using the equation

$$N_{excess} = N_{ON} - \alpha N_{OFF}, \tag{4}$$

where N_{ON} and N_{OFF} are the counts in the ON and OFF regions, respectively, and α is the ratio between the acceptances for the ON and OFF regions. The binned *excess* counts are the data used to create science products (DL5).

3.2.2 Point-Source Background Validation

Before continuing with the analysis, it is important to ensure that the background estimation is working as intended. In order to validate the background method, the ON region (source region) was placed off the source. The exclusion mask was kept in place over the source position to prevent contamination. When the ON region is on the source, significant counts are expected. When the ON region is off the source, we expect few excess counts and a low significance, within one standard deviation of the total counts, defined to be the square root of the counts in the ON region. Significance is the $\sqrt{TS}$ Li and Ma significance [12] [17], and is required to be 5σ or greater for a significant detection. Table 1 displays the results of the background validation, which are consistent with our expectations for a correctly estimated background. The geometry of the validation regions are shown in Fig. 4

On Source?	Counts	Background	Excess	Significance
Yes	31286	652.895	30633.105	368.033
No	626	617.024	8.976	0.357
No	620	621.732	-1.732	-0.0688

Table 1: *The results of the background validation. This method shows a very significant detection when the ON region is on the source, and a lack of significant detections when the ON region is off the source*

3.2.3 Spectral Fitting and Flux Points

Before estimating a light curve, it is necessary to generate a spectral model for the source. This is done by fitting a spectral model to the reduced datasets, binned along the energy axis. For Markarian 421, an Exponential Cutoff Power Law model was used, described by the equation [4]

$$\phi(E) = \phi_0 \cdot \left(\frac{E}{E_0}\right)^{-\Gamma} \exp\left(-(\lambda E)^{\alpha}\right), \tag{5}$$

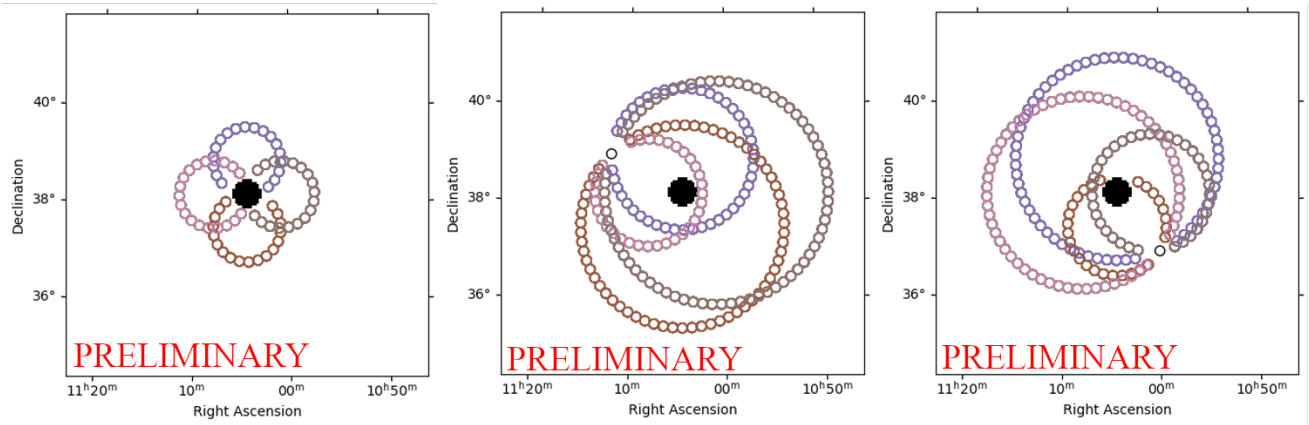

Figure 4: *Left: Geometry of the Reflected Regions background method when on source. Center, Right: Geometry of the background validation cases. In both cases, the small black circle is the ON region, and the small colored circles are the OFF regions. Each ring of OFF regions represents an observation at a "wobbled" position. In the on-source case, the ON region is obscured by the exclusion mask (large filled black circle).*

where ϕ_o is the flux normalization factor, Γ is the spectral index, E_0 is the reference energy, and λ is the energy-dependent attenuation. Additionally, it is essential to take into account attenuation of gamma-rays from the Extragalactic Background Light (EBL) via pair production. To do so, the spectral model was multiplied by an EBL model to model spectral absorption. For this analysis, the Domínguez 2011 [11] model was used, and is available in Gammapy. The fit results are described in Table 2.

Parameter	Value	Uncertainty	Unit	Frozen?
ϕ_0	1.2543	0.0381	$\frac{photons}{TeV \cdot s \cdot cm^2}$	No
E_0	1	N/A	TeV	Yes
Γ	1.7282	0.0151	N/A	No
λ	1.1710	0.0298	TeV^{-1}	No
α	1	N/A	N/A	Yes

Table 2: *Fit results for the spectrum of Markarian 421, fit with an Exponential Cutoff Power Law.*

After the creation of a spectral model, a flux spectrum can be generated. The spectral model is used to estimate flux points within the defined bins along the energy axis using Gammapy's provided estimators. The flux spectrum is shown in Fig. 5.

3.3 Variability Analysis

3.3.1 Goals

Once the preliminary analysis was complete, the spectral model could now be used to generate light curves, and test for variability. The goal of this variability analysis was to test for variability on a variety of timescales and determine the smallest timescale on which CTAO could detect significant variability for Markarian 421.

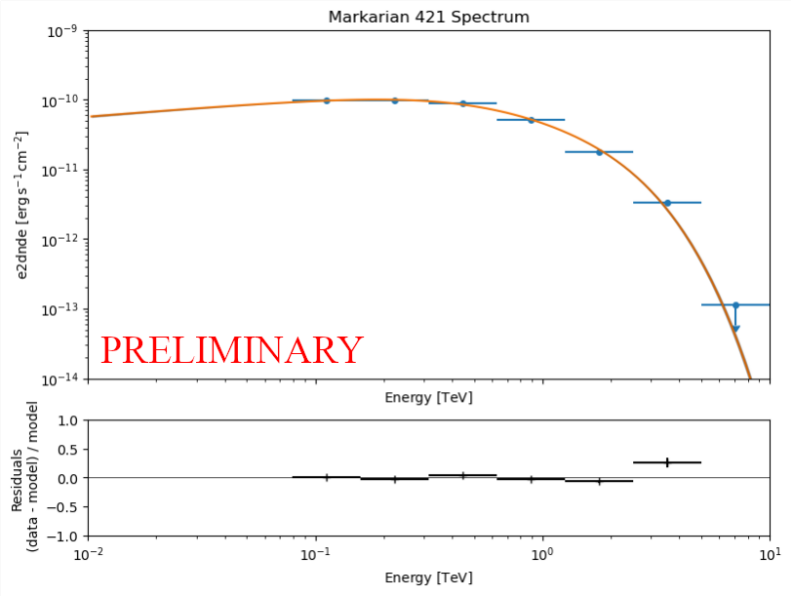

Figure 5: *Flux spectrum of Markarian 421. Estimated flux points are shown in blue, and the model is shown in yellow*

3.3.2 Testing for Variability

Variability was tested using a χ^2 test on a constant flux fit, using a method introduced in [1]. The χ^2 statistic is given by

$$\chi^2 = \sum_{i=1}^{N_p} \frac{(F_i - \langle F \rangle)^2}{\sigma_i^2}, \tag{6}$$

where F_i is the flux in a certain time bin, σ_i is the uncertainty in the flux, and N_p is the number of time bins in the light curve. The p-value is found for a χ^2 distribution with $N_p - 1$ degrees of freedom. The p-value represents the probability that the flat line represents the data, therefore the inverse, $1 - p$, is the probability that the flat line does not represent the data. Variability is then defined as the inability to represent the data with a constant flux model. The Variability Probability is $1 - p$, defined as the probability that the light curve contains variability. The light curve is defined to exhibit significant variability above a variability probability of 95%.

3.3.3 Long Timescales

For long timescales, here defined to be any longer than one 30-minute observing run, full observation-length bins were used. The 1-year light curve is shown in Fig 6, compared to the average flux fit. The light curve was tested for variability using the method described above, and a variability probability of 1 was found. The light curve was then split into months, leaving 3-4 observing runs per month, for a total of 12-16 bins. The 1-month light curves are displayed in Fig. 7. The χ^2 test for variability was performed on each 1-year light curve, calculating a new average flux each time.The average variability probability between all months during which data was collected was found to be 0.99927.

3.3.4 Short Timescales

Unfortunately, the simulated Long-Term Monitoring dataset was very sparse, so the next available time interval for analysis are individual 30-minute observing runs. After that, 15-minute (2-observation) and 7.5-minute (1-observation) intervals were tested. For all time intervals with lengths of 1 observing run or less, it was important to find the optimal bin size for analysis. Decreasing the bin size of a light curve can reveal shorter-timescale variability, as in the example

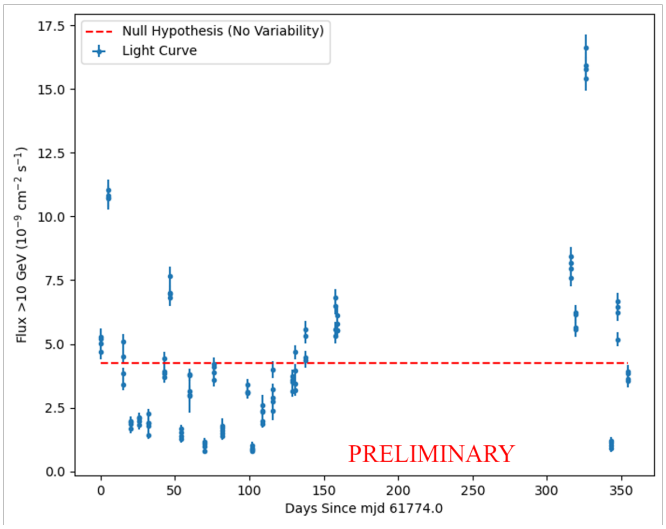

Figure 6: *1-year light curve compared with constant average flux. The light curve shows significant deviation from the constant flux. MJD 61774 corresponds to calendar date Jan 4, 2028.*

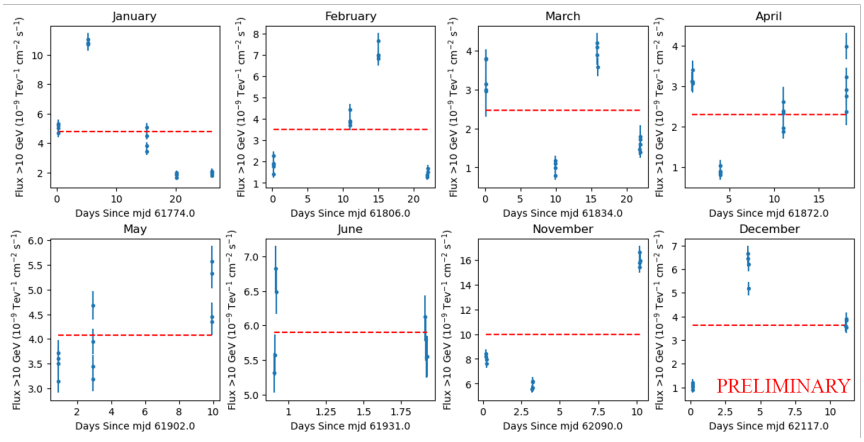

Figure 7: *1-month light curves, compared with constant average fluxes. Average flux was calculated for each time interval.*

in Fig 8. On average, this causes an increase in the variability probability, as shown in

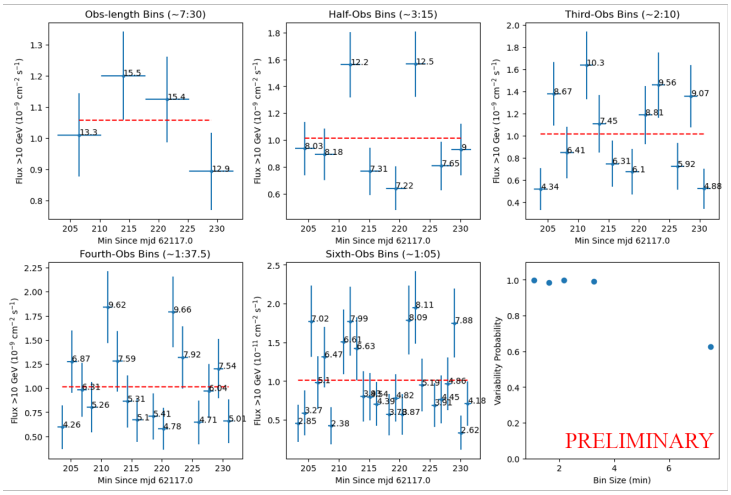

Figure 8: *Light curves of one 30-min observation run, plotted in the five different bin sizes. Also plotted is the variability probability for each bin size.*

Fig 9. However, decreasing the bin size also decreases the counts measured in each bin, and thus

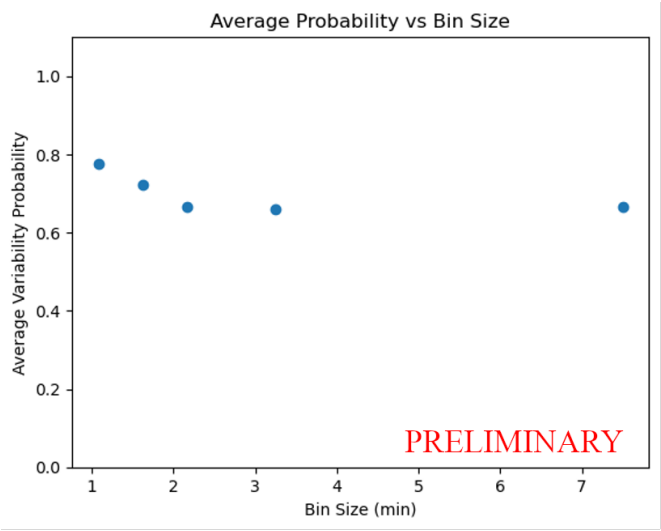

Figure 9: *Average variability probability for all 30-minute light curves at each bin size. This plot shows that as the bin size decreases, the variability probability increases on average.*

the significance of each point on the light curve, potentially below the criteria for a significant detection. The optimal bin size for testing is then the smallest bin size (to maximize variability) that fulfills the significance criteria. The significance criteria was set such that at least 80% of the points in each light curve must have a a significance greater than 5σ, ensuring that a large majority of points are considered significant detections of the source. The bin sizes tested for this criterion are 7.5 minutes, 3 minutes 15 seconds, 2 minutes 10 seconds, 1 minute 37.5 seconds, and 1 minute 5 seconds. The shorter bins are subdivisions of 6.5 minutes. These were chosen because when the observations were broken up into smaller bins, it was discovered that there was 1 minute of downtime at the end of each observation, most likely used to reposition the telescope. This last minute was cut off of the original observations when splitting into multiple sub-observation bins. To find the optimal bin size, the smallest bin size was tested against the significance criteria first. If this light curve passes the criteria, its variability probability is calculated. If not, the next largest bin size is tested, until a light curve bin size is found that satisfies the criteria.

3.3.5 Results

The average variability probability was calculated, and the results are shown in Fig 10. Average variability probability decreases on shorter timescales, dropping below 95 % at some point between 30 minutes and 1 month. Unfortunately, due to the sparsity of this data the threshold is not clear. However, we can safely say that if CTAO wants to more consistently look for short-timescale variability in Markarian 421, they should observe the source for more than 30 minutes per week, i.e., for longer than 30 minutes and more frequently than once per week.

3.3.6 Special Cases

Despite an insignificant average variability probability, a few 30-min observing runs did exhibit consistent high variability probability of 95 % or greater. Within these runs, I looked for potential flaring activity, qualitatively evidenced by rise-and-fall trends in flux, or one of the two. Two runs were selected and fit with exponential functions.

Run 2, simulated to have taken place on Jan 19, 2028, displayed a distinct decreasing pattern in its light curve. The light curve was fit with an exponential decay function,

$$F(t) = F_0 e^{\frac{-(t-t_0)}{t_{decay}}}, \tag{7}$$

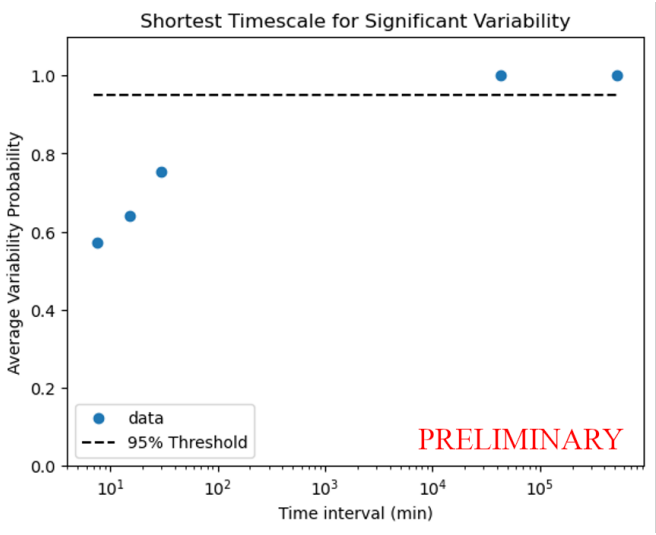

Figure 10: *Results of the variability testing of 5 time intervals: 1 year, 1 month, 30 minutes, 15 minutes, and 7.5 minutes. Optimal binning was performed on every time interval with a length of 30 minutes or less. There is a clear, large gap between the 1-month and 30-minute time intervals. The data reaches the 95% threshold for significance somewhere within that gap.*

including a peak time, t_0, and peak flux, F_0, as well as a characteristic timescale, t_{decay}. In order to reduce degeneracy in the fit and get a better picture of the decay time, t_0 was set at the start of the first observation. This fit was also compared to a flat-line (average flux) fit with a likelihood ratio test (find a source for this and cite it here). Light curves of every bin size were fit except for full, 7.5-min bins, which was not fit because it did not contain enough data points. The results of the fits are displayed in Table 3. The best fit was with the 3:15-minute bins, shown

Bin size (min)	F_0 $(10^{-9}\frac{photons}{s\cdot cm^2})$	ΔF_0 $(10^{-9}\frac{photons}{s\cdot cm^2})$	t_{decay} **(min)**	Δt_{decay} **(min)**	$\sqrt{TS}$
3:15	5.29	0.21	47.7	6.0	1.952
2:10	5.29	0.33	46.3	8.9	1.586
1:37.5	5.27	0.27	47.0	7.6	1.353
1:05	5.20	0.32	46.8	9.0	1.106

Table 3: *Fit results for the exponential fall fit of the special case of high variability probability on Jan 19, 2028 for all bin sizes.*

in Fig. 11. This fit resulted in a decay timescale of 47.7 ± 5.9 minutes. Using Eq. 2, this results in an upper limit of the ratio between the radius of the spherical emission region and Doppler factor of $\frac{R}{\delta} \leq 8.335 \times 10^{11}\text{m} = 2.701 \times 10^{-5}$parsecs.

Run 25, simulated to have taken place on Dec 12, 2028 qualitatively displayed a two-burst rise and fall pattern in its light curve, revealed as the bin size was decreased. However, the 1-minute 5-second bins did not meet the significance criterion defined in the variability analysis, so only the light curve with 1-minute 37.5-second bins was analyzed. It was fit with a piecewise exponential-rise-and-fall function for two consecutive flares,

$$F(t) = \begin{cases} F_0 e^{\frac{(t-t_{peak0})}{t_{rise0}}} & t < t_{peak0} \\ F_0 e^{\frac{-(t-t_{peak0})}{t_{decay0}}} & t_{peak0} \leq t < t_{split} \\ F_1 e^{\frac{(t-t_{peak1})}{t_{rise1}}} & t_{split} \leq t < t_{peak0} \\ F_1 e^{\frac{-(t-t_{peak1})}{t_{decay1}}} & t \geq t_{peak1} \end{cases}, \tag{8}$$

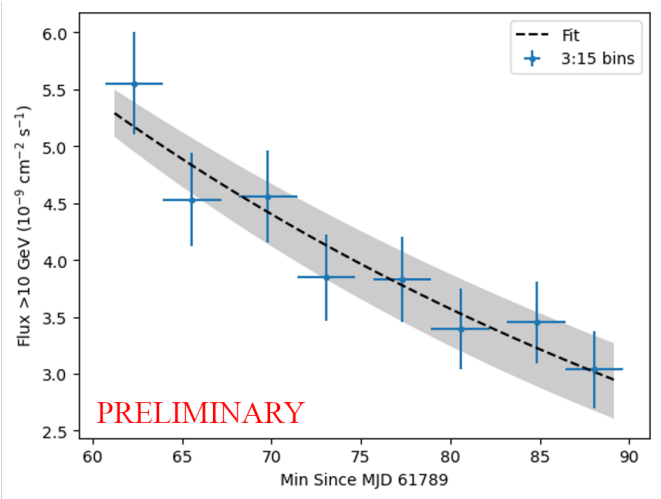

Figure 11: *Special case of high variability observed on Jan 19, 2028, showing a distinct fall in flux. This light curve was fit with the exponential fall function described by Eq. 7*

where F_0 and F_1 are the peak fluxes, t_{peak0} and t_{peak1} are the peak times, t_{rise0} and t_{rise1} are the rise timescales, t_{decay0} and t_{decay1} are the decay timescales, and t_{split} denotes the end of the first burst and the start of the second.

The fit result is displayed in Table 4, and is plotted in Fig 12. The characteristic timescale for the first burst is the decay timescale, found to be 4.9 ± 3.9 minutes. The characteristic timescale for the second burst is the rise timescale, found to be 3.2 ± 2.1 minutes. It is worth noting that these results do have large uncertainties, most likely due to a lack of data points in the 1-minute 37.5-second binned light curve compared to the large number of fit parameters. This observing run had a low average flux, which resulted in some 1-minute 5-second bins having a significance too low to be considered significant detections, which necessitated moving up to 1-minute 37.5-second bins. The characteristic timescales of the first and second peak resulted in upper limits on $\frac{R}{\delta}$ of $8.48 \times 10^{10} m = 2.75 \times 10^{-6}$parsecs and $5.61 \times 10^{10} m = 1.82 \times 10^{-6}$parsecs, respectively.

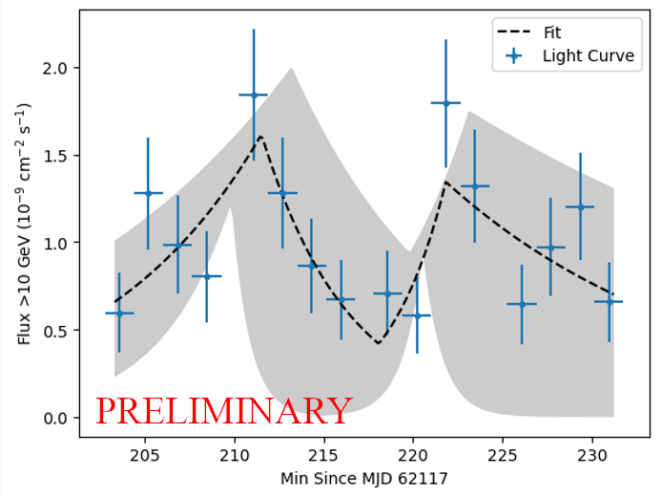

Figure 12: *Special case of high variability observed on Dec 12, 2028, showing a two-peak flare shape. This light curve was fit with the piecewise exponential function described by Eq. 8*

Parameter	Value	Uncertainty	Unit	Parameter	Value	Uncertainty	Unit
F_0	1.61	0.39	$\frac{photons}{s \cdot cm^2}$	F_1	1.34	0.41	$\frac{photons}{s \cdot cm^2}$
t_{peak0}	211.5	1.7	min	t_{peak1}	221.8	1.3	min
t_{rise0}	9.1	5.3	min	t_{rise1}	3.2	2.1	min
t_{decay0}	4.9	3.9	min	t_{decay1}	14.4	13.3	min
t_{split}	218.1		min	$\sqrt{TS}$	1.660		

Table 4: *Fit results for the piecewise exponential fit of the double-peaked flaring activity on Dec 12, 2028.*

4 Conclusions

4.1 Variability Analysis

We successfully analyzed one year of simulated CTAO data using Gammapy, fulfilling a goal of the SDC. In doing so, we developed an analysis pipeline for generating light curves for a variety of different time intervals, as well as different bin sizes. Utilizing a variability testing method described in literature, we were able to quantify the probability of the presence of variability and assess it over different timescales. It was observed that, as expected, the average variability probability decreased over shorter timescales. However, the variability probability for small intervals could be increased on average by decreasing the bin size, given that the bins remained significant. To find this optimal bin size, a method was developed to find the smallest bin size that fulfilled the significance criteria. Unfortunately, the dataset was too sparse to accurately determine the threshold at which the average variability probability became significant (95%). However, we can safely conclude that if CTAO wants to more consistently observe short-timescale variability in Mrk 421, it should observe for more than 30 minutes per week.

4.2 Special Cases

Despite the average being insignificant, there were some cases of short-timescale variability observed, and two of those exhibited possible flaring activity. Those flares were fit with exponential functions with characteristic timescales. For the strictly falling case, a decay timescale of 47.7 minutes was found. For the double-peaked case, even shorter variability timescales were found, on the order of a few minutes. Both of these timescales are very short, and suggest very small emission regions by Eq. 2. These timescales and small emission regions continue to support the idea that emission is associated with small regions within the blazar jet [22]. Additionally, the decay timescale for the exponential fall case is consistent with particle cooling timescales due to radiative losses from Inverse Compton Scattering. The presence of Inverse Compton Scattering then suggests that the emission mechanisms are leptonic [22]. For the double-peaked case, the asymmetry of the flares can provide clues about their causes. For the first burst, the longer rise than fall timescale is consistent with an injection of high-energy particles into the emission region, causing the flare, with the abrupt fall being a result of cessation of the injection. On the other hand, the second burst has a much shorter rise time than fall time, which is more consistent with *in situ* acceleration of particles in the emitting region, and longer cooling than variability timescales associated with steeper particle-energy distributions, since lower-energy particles take more time to cool[2].

5 Acknowledgements

This material is based upon work supported by the National Science Foundation under Grant No. PHY-2349438. I would like to thank Professor Reshmi Mukherjee, Dr. Ruo yu Shang, and the rest of the VERITAS/CTAO group at Nevis Labs for their support and guidance on this project, without which this project would not have been possible. I would also like to thank Professor Reshmi Mukherjee, Professor Georgia Karagiorgi, Amy Garwood, and the rest of the Nevis staff for running an incredible REU program. Finally, I would like to thank my fellow REU participants and everyone else at Nevis for making this such a fun and educational summer.

References

[1] A. A. Abdo, M. Ackermann, M. Ajello, E. Antolini, L. Baldini, J. Ballet, G. Barbiellini, D. Bastieri, K. Bechtol, R. Bellazzini, B. Berenji, R. D. Blandford, E. D. Bloom, E. Bonamente, A. W. Borgland, A. Bouvier, J. Bregeon, A. Brez, M. Brigida, P. Bruel, R. Buehler, T. H. Burnett, S. Buson, G. A. Caliandro, R. A. Cameron, P. A. Caraveo, S. Carrigan, J. M. Casandjian, E. Cavazzuti, C. Cecchi, Ö. Çelik, A. Chekhtman, C. C. Cheung, J. Chiang, S. Ciprini, R. Claus, J. Cohen-Tanugi, L. R. Cominsky, J. Conrad, L. Costamante, S. Cutini, C. D. Dermer, A. de Angelis, F. de Palma, E. do Couto e Silva, P. S. Drell, R. Dubois, D. Dumora, C. Farnier, C. Favuzzi, S. J. Fegan, W. B. Focke, P. Fortin, M. Frailis, Y. Fukazawa, S. Funk, P. Fusco, F. Gargano, D. Gasparrini, N. Gehrels, S. Germani, B. Giebels, N. Giglietto, P. Giommi, F. Giordano, T. Glanzman, G. Godfrey, I. A. Grenier, M.-H. Grondin, J. E. Grove, S. Guiriec, D. Hadasch, M. Hayashida, E. Hays, S. E. Healey, D. Horan, R. E. Hughes, R. Itoh, G. Jóhannesson, A. S. Johnson, W. N. Johnson, T. Kamae, H. Katagiri, J. Kataoka, N. Kawai, J. Knödlseder, M. Kuss, J. Lande, S. Larsson, L. Latronico, M. Lemoine-Goumard, F. Longo, F. Loparco, B. Lott, M. N. Lovellette, P. Lubrano, G. M. Madejski, A. Makeev, E. Massaro, M. N. Mazziotta, J. E. McEnery, P. F. Michelson, W. Mitthumsiri, T. Mizuno, A. A. Moiseev, C. Monte, M. E. Monzani, A. Morselli, I. V. Moskalenko, M. Mueller, S. Murgia, P. L. Nolan, J. P. Norris, E. Nuss, M. Ohno, T. Ohsugi, N. Omodei, E. Orlando, J. F. Ormes, M. Ozaki, J. H. Panetta, D. Parent, V. Pelassa, M. Pepe, M. Pesce-Rollins, F. Piron, T. A. Porter, S. Rainò, R. Rando, M. Razzano, A. Reimer, O. Reimer, S. Ritz, A. Y. Rodriguez, R. W. Romani, M. Roth, F. Ryde, H. F.-W. Sadrozinski, A. Sander, J. D. Scargle, C. Sgrò, M. S. Shaw, P. D. Smith, G. Spandre, P. Spinelli, J.-L. Starck, M. S. Strickman, D. J. Suson, H. Takahashi, T. Takahashi, T. Tanaka, J. B. Thayer, J. G. Thayer, D. J. Thompson, L. Tibaldo, D. F. Torres, G. Tosti, A. Tramacere, Y. Uchiyama, T. L. Usher, V. Vasileiou, N. Vilchez, V. Vitale, A. P. Waite, E. Wallace, P. Wang, B. L. Winer, K. S. Wood, Z. Yang, T. Ylinen, and M. Ziegler. Gamma-ray light curves and variability of bright fermi-detected blazars. *The Astrophysical Journal*, 722(1):520, sep 2010.

[2] A. U. Abeysekara, W. Benbow, R. Bird, T. Brantseg, R. Brose, M. Buchovecky, J. H. Buckley, V. Bugaev, M. P. Connolly, W. Cui, M. K. Daniel, A. Falcone, Q. Feng, J. P. Finley, L. Fortson, A. Furniss, G. H. Gillanders, I. Gunawardhana, M. Hütten, D. Hanna, O. Hervet, J. Holder, G. Hughes, T. B. Humensky, C. A. Johnson, P. Kaaret, P. Kar, M. Kertzman, F. Krennrich, M. J. Lang, T. T. Y. Lin, S. McArthur, P. Moriarty, R. Mukherjee, S. O'Brien, R. A. Ong, A. N. Otte, N. Park, A. Petrashyk, M. Pohl, E. Pueschel, J. Quinn, K. Ragan, P. T. Reynolds, G. T. Richards, E. Roache, C. Rulten, I. Sadeh, M. Santander, G. H. Sembroski, K. Shahinyan, S. P. Wakely, A. Weinstein, R. M. Wells, P. Wilcox, D. A. Williams, B. Zitzer, (The VERITAS Collaboration), S. G. Jorstad, A. P. Marscher, M. L. Lister, Y. Y. Kovalev, A. B. Pushkarev, T. Savolainen, I. Agudo, S. N. Molina, J. L. Gómez, V. M. Larionov, G. A. Borman, A. A. Mokrushina, M. Tornikoski, A. Lähteenmäki, W. Chamani, S. Enestam, S. Kiehlmann, T. Hovatta, P. S. Smith, and P. Pontrelli. Multiwavelength observations of the blazar bl lacertae: A new fast tev gamma-ray flare. *The Astrophysical Journal*, 856(2):95, mar 2018.

[3] A. U. Abeysekara, W. Benbow, R. Bird, A. Brill, R. Brose, M. Buchovecky, J. H. Buckley, J. L. Christiansen, A. J. Chromey, M. K. Daniel, J. Dumm, A. Falcone, Q. Feng, J. P. Finley, L. Fortson, A. Furniss, N. Galante, A. Gent, G. H. Gillanders, C. Giuri, O. Gueta, T. Hassan, O. Hervet, J. Holder, G. Hughes, T. B. Humensky, C. A. Johnson, P. Kaaret, P. Kar, N. Kelley-Hoskins, M. Kertzman, D. Kieda, M. Krause, F. Krennrich, S. Kumar, M. J. Lang, P. Moriarty, R. Mukherjee, T. Nelson, D. Nieto, M. Nievas-Rosillo, S. O'Brien, R. A. Ong, A. N. Otte, N. Park, A. Petrashyk, A. Pichel, M. Pohl, R. R. Prado, E. Pueschel,

J. Quinn, K. Ragan, P. T. Reynolds, G. T. Richards, E. Roache, A. C. Rovero, C. Rulten, I. Sadeh, M. Santander, G. H. Sembroski, K. Shahinyan, B. Stevenson, I. Sushch, J. Tyler, V. V. Vassiliev, S. P. Wakely, A. Weinstein, R. M. Wells, P. Wilcox, A. Wilhelm, D. A. Williams, B. Zitzer, V. A. Acciari, S. Ansoldi, L. A. Antonelli, A. Arbet Engels, D. Baack, A. Babić, B. Banerjee, U. Barres de Almeida, J. A. Barrio, J. Becerra González, W. Bednarek, L. Bellizzi, E. Bernardini, A. Berti, J. Besenrieder, W. Bhattacharyya, C. Bigongiari, A. Biland, O. Blanch, G. Bonnoli, G. Busetto, R. Carosi, G. Ceribella, Y. Chai, S. Cikota, S. M. Colak, U. Colin, E. Colombo, J. L. Contreras, J. Cortina, S. Covino, V. D'Elia, P. Da Vela, F. Dazzi, A. De Angelis, B. De Lotto, M. Delfino, J. Delgado, F. Di Pierro, E. Do Souto Espiñera, D. Dominis Prester, D. Dorner, M. Doro, S. Einecke, D. Elsaesser, V. Fallah Ramazani, A. Fattorini, A. Fernández-Barral, G. Ferrara, D. Fidalgo, L. Foffano, M. V. Fonseca, L. Font, C. Fruck, D. Galindo, S. Gallozzi, R. J. García López, M. Garczarczyk, S. Gasparyan, M. Gaug, N. Godinović, D. Green, D. Guberman, D. Hadasch, A. Hahn, J. Herrera, J. Hoang, D. Hrupec, S. Inoue, K. Ishio, Y. Iwamura, H. Kubo, J. Kushida, A. Lamastra, D. Lelas, F. Leone, E. Lindfors, S. Lombardi, F. Longo, M. López, R. López-Coto, A. López-Oramas, B. Machado de Oliveira Fraga, C. Maggio, P. Majumdar, M. Makariev, M. Mallamaci, G. Maneva, M. Manganaro, K. Mannheim, L. Maraschi, M. Mariotti, M. Martínez, S. Masuda, D. Mazin, D. Miceli, M. Minev, J. M. Miranda, R. Mirzoyan, E. Molina, A. Moralejo, D. Morcuende, V. Moreno, E. Moretti, P. Munar-Adrover, V. Neustroev, A. Niedzwiecki, M. Nievas Rosillo, C. Nigro, K. Nilsson, D. Ninci, K. Nishijima, K. Noda, L. Nogués, M. Nöthe, S. Paiano, J. Palacio, M. Palatiello, D. Paneque, R. Paoletti, J. M. Paredes, P. Peñil, M. Peresano, M. Persic, P. G. Prada Moroni, E. Prandini, I. Puljak, W. Rhode, M. Ribó, J. Rico, C. Righi, A. Rugliancich, L. Saha, N. Sahakyan, T. Saito, K. Satalecka, T. Schweizer, J. Sitarek, I. Šnidarić, D. Sobczynska, A. Somero, A. Stamerra, D. Strom, M. Strzys, S. Sun, T. Surić, F. Tavecchio, P. Temnikov, T. Terzić, M. Teshima, N. Torres-Albà, S. Tsujimoto, J. van Scherpenberg, G. Vanzo, M. Vazquez Acosta, I. Vovk, M. Will, D. Zarić, H. D. Aller, M. F. Aller, M. T. Carini, D. Horan, B. Jordan, S. G. Jorstad, O. M. Kurtanidze, S. O. Kurtanidze, A. Lähteenmäki, V. M. Larionov, E. G. Larionova, G. Madejski, A. P. Marscher, W. Max-Moerbeck, J. Ward Moody, D. A. Morozova, M. G. Nikolashvili, C. M. Raiteri, A. C. S. Readhead, J. L. Richards, A. C. Sadun, T. Sakamoto, L. A. Sigua, P. S. Smith, H. Talvikki, J. Tammi, M. Tornikoski, I. S. Troitsky, and M. Villata. The great markarian 421 flare of 2010 february: Multiwavelength variability and correlation studies. *The Astrophysical Journal*, 890(2):97, February 2020.

[4] Fabio Acero, Juan Bernete, Noah Biederbeck, Julia Djuvsland, Axel Donath, Kirsty Feijen, Stefan Fröse, Claudio Galelli, Bruno Khélifi, Jana Konrad, Paula Kornecki, Maximilian Linhoff, Kurt McKee, Simone Mender, Daniel Morcuende, Laura Olivera-Nieto, Fabio Pintore, Michael Punch, Maxime Regeard, Quentin Remy, Atreyee Sinha, Hanna Stapel, Katrin Streil, Régis Terrier, and Tim Unbehaun. Gammapy v1.2: Python toolbox for gamma-ray astronomy, 02 2024.

[5] F. Aharonian, A. G. Akhperjanian, A. R. Bazer-Bachi, B. Behera, M. Beilicke, W. Benbow, D. Berge, K. Bernlöhr, C. Boisson, O. Bolz, V. Borrel, T. Boutelier, I. Braun, E. Brion, A. M. Brown, R. Bühler, I. Büsching, T. Bulik, S. Carrigan, P. M. Chadwick, A. C. Clapson, L. M. Chounet, G. Coignet, R. Cornils, L. Costamante, B. Degrange, H. J. Dickinson, A. Djannati-Ataï, W. Domainko, L. O'C. Drury, G. Dubus, J. Dyks, K. Egberts, D. Emmanoulopoulos, P. Espigat, C. Farnier, F. Feinstein, A. Fiasson, A. Förster, G. Fontaine, Seb. Funk, S. Funk, M. Füßling, Y. A. Gallant, B. Giebels, J. F. Glicenstein, B. Glück, P. Goret, C. Hadjichristidis, D. Hauser, M. Hauser, G. Heinzelmann, G. Henri, G. Hermann, J. A. Hinton, A. Hoffmann, W. Hofmann, M. Holleran, S. Hoppe, D. Horns, A. Jacholkowska, O. C. de Jager, E. Kendziorra, M. Kerschhaggl, B. Khélifi, Nu. Komin, K. Kosack, G. Lamanna, I. J. Latham, R. Le Gallou, A. Lemière, M. Lemoine-Goumard, J. P. Lenain, T. Lohse, J. M.

Martin, O. Martineau-Huynh, A. Marcowith, C. Masterson, G. Maurin, T. J. L. McComb, R. Moderski, E. Moulin, M. de Naurois, D. Nedbal, S. J. Nolan, J. P. Olive, K. J. Orford, J. L. Osborne, M. Ostrowski, M. Panter, G. Pedaletti, G. Pelletier, P. O. Petrucci, S. Pita, G. Pühlhofer, M. Punch, S. Ranchon, B. C. Raubenheimer, M. Raue, S. M. Rayner, M. Renaud, J. Ripken, L. Rob, L. Rolland, S. Rosier-Lees, G. Rowell, B. Rudak, J. Ruppel, V. Sahakian, A. Santangelo, L. Saugé, S. Schlenker, R. Schlickeiser, R. Schröder, U. Schwanke, S. Schwarzburg, S. Schwemmer, A. Shalchi, H. Sol, D. Spangler, Ł. Stawarz, R. Steenkamp, C. Stegmann, G. Superina, P. H. Tam, J. P. Tavernet, R. Terrier, C. van Eldik, G. Vasileiadis, C. Venter, J. P. Vialle, P. Vincent, M. Vivier, H. J. Völk, F. Volpe, S. J. Wagner, M. Ward, and A. A. Zdziarski. An Exceptional Very High Energy Gamma-Ray Flare of PKS 2155-304. *Astrophysical Journal*, 664(2):L71–L74, August 2007.

[6] Aharonian, F., Akhperjanian, A., Barrio, J., Bernlöhr, K., Börst, H., Bojahr, H., Bolz, O., Contreras, J., Cortina, J., Denninghoff, S., Fonseca, V., Gonzalez, J., Götting, N., Heinzelmann, G., Hermann, G., Heusler, A., Hofmann, W., Horns, D., Ibarra, A., Iserlohe, C., Jung, I., Kankanyan, R., Kestel, M., Kettler, J., Kohnle, A., Konopelko, A., Kornmeyer, H., Kranich, D., Krawczynski, H., Lampeitl, H., Lopez, M., Lorenz, E., Lucarelli, F., Magnussen, N., Mang, O., Meyer, H., Mirzoyan, R., Moralejo, A., Ona, E., Padilla, L., Panter, M., Plaga, R., Plyasheshnikov, A., Prahl, J., Pühlhofer, G., Rauterberg, G., Röhring, A., Rhode, W., Rowell, G. P., Sahakian, V., Samorski, M., Schilling, M., Schröder, F., Siems, M., Stamm, W., Tluczykont, M., Völk, H. J., Wiedner, C. A., and Wittek, W. Evidence for tev gamma ray emission from cassiopeia a. *Astronomy & Astrophysics*, 370(1):112–120, 2001.

[7] Alex Sidler. Analyzing simulated very high energy gamma-ray data from dark matter annihilation. `https://www.nevis.columbia.edu/reu/2024/`, 2024. Accessed: 2025-08-09.

[8] Volker Beckmann and Chris SHRADER. The AGN phenomenon: open issues. *PoS*, INTEGRAL 2012:069, 2013.

[9] D. Berge, S. Funk, and J. Hinton. Background modelling in very-high-energy γ-ray astronomy. *Astronomy & Astrophysics*, 466(3):1219–1229, May 2007.

[10] Matteo Cerruti. Leptonic and hadronic radiative processes in supermassive-black-hole jets. *Galaxies*, 8(4):72, October 2020.

[11] A. Domínguez, J. R. Primack, D. J. Rosario, F. Prada, R. C. Gilmore, S. M. Faber, D. C. Koo, R. S. Somerville, M. A. Pérez-Torres, P. Pérez-González, J. S. Huang, M. Davis, P. Guhathakurta, P. Barmby, C. J. Conselice, M. Lozano, J. A. Newman, and M. C. Cooper. Extragalactic background light inferred from AEGIS galaxy-SED-type fractions. *MNRAS*, 410(4):2556–2578, February 2011.

[12] Donath, Axel, Terrier, Régis, Remy, Quentin, Sinha, Atreyee, Nigro, Cosimo, Pintore, Fabio, Khélifi, Bruno, Olivera-Nieto, Laura, Ruiz, Jose Enrique, Brügge, Kai, Linhoff, Maximilian, Contreras, Jose Luis, Acero, Fabio, Aguasca-Cabot, Arnau, Berge, David, Bhattacharjee, Pooja, Buchner, Johannes, Boisson, Catherine, Carreto Fidalgo, David, Chen, Andrew, de Bony de Lavergne, Mathieu, de Miranda Cardoso, José Vinicius, Deil, Christoph, Füßling, Matthias, Funk, Stefan, Giunti, Luca, Hinton, Jim, Jouvin, Léa, King, Johannes, Lefaucheur, Julien, Lemoine-Goumard, Marianne, Lenain, Jean-Philippe, López-Coto, Rubén, Mohrmann, Lars, Morcuende, Daniel, Panny, Sebastian, Regeard, Maxime, Saha, Lab, Siejkowski, Hubert, Siemiginowska, Aneta, Sipőcz, Brigitta M., Unbehaun, Tim, van Eldik, Christopher, Vuillaume, Thomas, and Zanin, Roberta. Gammapy: A python package for gamma-ray astronomy. *Astronomy & Astrophysics*, 678:A157, 2023.

[13] Manel Errando and Takayuki Saito. *How to Detect Gamma Rays from Ground: An Introduction to the Detection Concepts*, pages 1–37. Springer Nature Singapore, Singapore, 2022.

[14] J. A. Gaidos, C. W. Akerlof, S. Biller, P. J. Boyle, A. C. Breslin, J. H. Buckley, D. A. Carter-Lewis, M. Catanese, M. F. Cawley, D. J. Fegan, J. P. Finley, J. Bussöns Gordo, A. M. Hillas, F. Krennrich, R. C. Lamb, R. W. Lessard, J. E. McEnery, C. Masterson, G. Mohanty, P. Moriarty, J. Quinn, A. J. Rodgers, H. J. Rose, F. Samuelson, M. S. Schubnell, G. H. Sembroski, R. Srinivasan, T. C. Weekes, C. L. Wilson, and J. Zweerink. Extremely rapid bursts of TeV photons from the active galaxy Markarian 421. *Nature*, 383(6598):319–320, 1996.

[15] David Hanna and Reshmi Mukherjee. *The Very Energetic Radiation Imaging Telescope Array System (VERITAS)*, page 2703–2743. Springer Nature Singapore, 2024.

[16] Werner Hofmann and Roberta Zanin. The Cherenkov Telescope Array. *arXiv e-prints*, page arXiv:2305.12888, May 2023.

[17] T. P. Li and Y. Q. Ma. Analysis methods for results in gamma-ray astronomy. *Astrophysical Journal*, 272:317–324, September 1983.

[18] Paul J Morris, William J Potter, and Garret Cotter. The feasibility of magnetic reconnection powered blazar flares from synchrotron self-compton emission. *Monthly Notices of the Royal Astronomical Society*, 486(2):1548–1562, 03 2019.

[19] S. Navas et al. Review of particle physics. *Phys. Rev. D*, 110(3):030001, 2024.

[20] M. Punch, C. W. Akerlof, M. F. Cawley, M. Chantell, D. J. Fegan, S. Fennell, J. A. Gaidos, J. Hagan, A. M. Hillas, Y. Jiang, A. D. Kerrick, R. C. Lamb, M. A. Lawrence, D. A. Lewis, D. I. Meyer, G. Mohanty, K. S. O'Flaherty, P. T. Reynolds, A. C. Rovero, M. S. Schubnell, G. Sembroski, T. C. Weekes, T. Whitaker, and C. Wilson. Detection of TeV photons from the active galaxy Markarian 421. *Nature*, 358(6386):477–478, 1992.

[21] Roberta Zanin. Will it make the boat go faster? - using ctao for science, 2024. Talk given at the 2nd CTAO Science Symposium in March 2024 in Bologna, Italy.

[22] Joni Tammi and Peter Duffy. Particle-acceleration time-scales in tev blazar flares. *Monthly Notices of the Royal Astronomical Society*, 393(3):1063–1069, 02 2009.